Inorganic nanocrystalline and hybrid nanocrystalline particles (Gamma-Fe2O3/PPY) and their contribution to electrode materials for lithium batteries

Chai-Won Kwon, Mathieu Quintin, Stéphane Mornet, C. Barbieri, Olivier Devos, Guy Campet, Marie-Hélène Delville

Inorganic nanocrystalline and hybrid nanocrystalline particles (gamma-Fe_2O_3/PPY) and their contribution to electrode materials for lithium batteries

C. W. Kwon,[a] M. Quintin,[a] S. Mornet,[a] C. Barbieri,[a] O. Devos,[a,b] G. Campet,[a] and M. H. Delville[a,z]

[a]*Institut de Chimie de la Matière Condensée de Bordeaux, ICMCB-UPR 9048-CNRS, Université Bordeaux 1, 33608 Pessac cedex, France*

[b]*Laboratoire Interfaces et Systèmes Electrochimique, LISE-UPR15-CNRS, Université Pierre et Marie Curie, 75252 Paris cedex 05, France*

Nanoscale materials offer the advantage of combining structural effects (inside grain structure) with surface effects or grain-boundary effects. Therefore, the electrochemistry of this type of materials is very different from that of traditional microcrystalline ones mainly due to the contribution of the 'surface defects' allowing strong coulombic interactions between the inserted lithium ions and the surface ions called 'electrochemical grafting'. When electrochemical grafting is the first electrochemical step to take place, it can favor the power density and the cycling life of electrode materials. As illustrative examples, electrochemical behaviors of nanocrystalline oxides such as $LiMn_2O_4$, γ-Fe_2O_3, and of nanohybrid inorganic-organic materials such as γ-Fe_2O_3/PPY (PPY = polypyrrole) are presented.

Humankind is becoming increasingly aware of the health and environmental effects of releasing noxious gases into the atmosphere due, for instance, to the transportation in big cities. Consequently, high energy and rechargeable power sources are needed for the development of long-range electric vehicles leading to the improvement of the air quality. On one hand, traditional lithium batteries based on well-crystallized host compounds such as the microcrystalline lamellar $LiCoO_2$ are considered to be the best choice,[1-7] together with fuel cells,[8] as they can provide high enough output power and lifetime. On the other hand, along with the progress of 'nanoscience', it was recently found that the nanoparticles electrochemical behavior is much different from that of microparticles because the former present a high density of surface defects.[9] Related to this aspect, using various examples (SnO_2, $LiNiO_2$, TiO_2), we have established the key conditions to obtain the cycling efficiency of these electrodes.[10-13] Nanocrystalline cathode materials were shown to exhibit an enhanced electrochemical activity, compared with their microcrystalline homologues, only when the first significant electrochemical step is an insertion of Li^+ ions (corresponding to a discharge of the Li battery). This insertion begins with the electrochemical grafting of Li^+ ions, promoted by structural defects at/near the nanocrystallite surface. This concept is illustrated in Fig. 1 showing a schematic band model for this grafting process.

The nanocrystalline materials present many sub-band-gap states between the conduction band and valence band originating from surface defects (distortion of coordination polyhedra, dangling bonds etc...). The cationic sub-band represents sub-band gap energy states arising from such structural defects. The first electrochemical Li^+ insertion process (process 1, Fig. 1) fills these localized sub-band-gap states, and consequently gives a smoother discharge curve as compared to the well-crystalline homologue. This gives a regular and smooth change of the Fermi-energy in the electrode without undergoing any significant structural change. Therefore, nanocrystalline materials can better adapt to structural phase transitions. This electrochemical grafting process (step 1) can be reversible, depending on the bond strength of the 'grafted' lithium ions. Moreover, as the cationic sub-band-gap states are progressively filled during the electrochemical grafting, the grain surface can be modified in such a way that the consecutive electrochemical processes 2 and 3, corresponding to electron injection in CB (Fig. 1), have enhanced reversibility.

[z] E-mail: delville@icmcb-bordeaux.cnrs.fr

The reverse trend logically occurs during the follow-up charge of the Li battery, *i.e.*, the electrochemical degrafting is the last step. This model, which highlights the surface effects, provides a useful insight to develop electrodes that are more efficient since it can foresee when it is preferable to consider nanocrystalline electrodes rather than their microcrystalline homologues. This is important for an industrial standpoint, because nanocrystalline materials can be advantageously prepared at low temperatures, using thereby low-cost synthetic processes. In this report, results are given on the surface effects of electrode materials based on the nanocrystalline oxides $LiMn_2O_4$, γ-Fe_2O_3.

The hybrid approach in materials science aims at the development of new materials based on the combination of organic and inorganic species in an attempt to obtain some reinforcement or synergy between them.[14] We illustrate this aspect with a special highlight on an organic-inorganic nanohybrid γ-Fe_2O_3/PPY (PPY = polypyrrole). This kind of polymer/transition metal oxide nanohybrid presents enhanced electronic conductivity linked to better grain separation. The redox active nature of both components offers promising possibilities in electrochemical applications such as positive materials in lithium batteries. For theses hybrid compounds, efficient n-p junctions are likely to occur at the core (γ-Fe_2O_3 n-type oxide)-shell (PPY p-type conductor) interface enhancing the overall electrochemical performances (synergy effect).

Experimental

Sample preparation and characterization.—The polycrystalline samples of $LiMn_2O_4$ with different particle sizes were prepared using two procedures: (*i*) the coprecipitation method, where an aqueous solution of $Mn(CH_3COO)_2 \cdot 4H_2O$ and Li_2CO_3 was stirred for 1 h and dehydrated at 85°C, and the resulting powder was heated at various temperatures (250 and 700°C) in an ambient atmosphere,[15] and (*ii*) an original polymeric route adapted to large-scale production. Homogeneous starting materials were obtained by addition of appropriate amounts of polyacrylamide (Paam), lithium carbonate and manganese (II) acetate tetrahydrate to an aqueous HNO_3 (1N) solution.[16] Both procedures yield similar results after controlled explosive redox reaction under oxygen atmosphere of the formed hybrid polymer leading to a fine powder of the spinel phase. The formation of single-phase $LiMn_2O_4$ spinel oxides was confirmed by X-ray diffraction (XRD) measurements using Ni-filtered CuKα radiation with a graphite diffracted beam monochromator.

The maghemite nanoparticles were prepared following the method developed by Massart *et al.*[17,18] First, magnetite (Fe_3O_4)

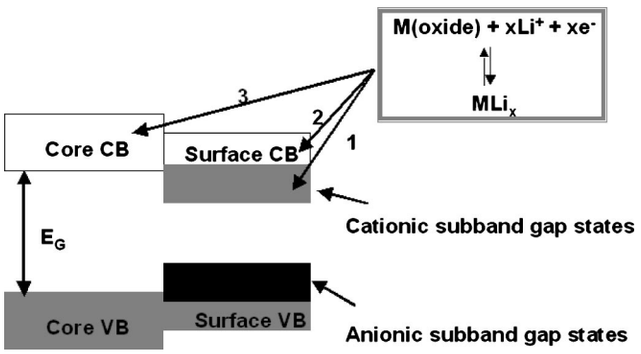

Figure 1. Schematic band model for the electrochemical grafting process.

was precipitated by alkalizing an aqueous iron chloride solution containing $Fe^{2+}/Fe^{3+} = 0.5$ with NH_4OH, leading to a magnetic colloid formation. In this reaction, the base nature, kinetics of reactants addition, concentration, temperature, stirring, precursors purity are all, significant parameters, which determine the product size distribution and phase. In a typical run, 143 mL of 2.21 M $FeCl_3$ aqueous solution (containing 316 mmol $FeCl_3$) and 170 mL 1.5 M HCl solution with 158 mmol $FeCl_2$ were prepared separately, and mixed with 3.5 L of distilled water. The solution was heated to 50°C. The addition of 300 mL of 8.6 M NH_4OH solution was followed by strong agitation for 15 min. This process gives ~36 g of Fe_3O_4 which is then oxidized to the more stable maghemite. The oxide nanoparticles surface is then acidified by replacing the flocculating counter-ions NH_4^+ by nitrate ions NO_3^- allowing, as well, their superficial oxidation. The final step consists of the addition of the particles to a ferric nitrate solution at boiling temperature. The product was washed four times with water and acetone and dried at 40°C. The surface area was *ca.* 130 m^2/g, measured by Brunauer Emmett, and Teller (BET) nitrogen adsorption method.

The maghemite/PPY hybrids were prepared as follows: 1.7 g of maghemite was dispersed in liquid pyrrole and excess pyrrole was removed. The remaining pyrrole was about 1.3 g. This mixture was added to 200 mL of a 0.15 M $FeCl_3$/ethanol solution under stirring. Polymerization lasted for 30 min, followed by filtration and washing with ethanol several times. The separation between modified maghemite and pristine polypyrrole was performed by decanting the modified maghemite particles in solution with a magnet. The polypyrrole, was removed by repeated washings with ethanol and acetone. Bulk polypyrrole (PPY) was also prepared, for comparison, with 1.3 g of pyrrole in the 200 mL of 0.30 M $FeCl_3$ ethanol solution for 4 h. The products were dried and preserved at 4°C.

Electrochemistry.—The electrochemical measurements were performed using a computer-controlled potentiostat/galvanostat (Tacussel, PGS 201T model) for the electrochemical cells based on the ''Li/liquid electrolyte/composite electrode''. The Li anode is a lithium metal foil (Aldrich 99.9%). The liquid electrolyte consists of 1 M $LiPF_6$ (Aldrich 99.99%) dissolved in a solution of ethylene carbonate (EC,Prolabo 99%) + dimethyl carbonate (DMC,Aldrich 99%) (50/50 vol.). The composite cathodes were prepared by mixing the lithium manganese oxide together with Chevron carbon black and a binder, polytetrafluoroethylene (PTFE), in the weight ratios 80:13:7. The mixture was then pressed at 1 ton/cm^2 for 1 min and the resulting pellet was finally dried under primary vacuum for 15 h at 120°C. The manipulation of air-sensitive materials and the cell assemblies were carried out in an argon-filled glove box.

For γ-Fe_2O_3 based materials, the composite electrodes were made by intimately mixing 71% (by mass) of the active material, 25% of Ketjenblack and 4% PTFE. The surface area of the electrodes and mass of active material were adjusted to 1 cm^2 and 20 mg, respectively, for reproducibility. These electrodes were dried under vacuum at 80°C, for 3 h, and introduced into an Argon-filled gloves box without any exposure to air. Charge/discharge experiments were carried out in a galvanostatic mode at 8 mA/g in the voltage range of 1.3-4.3 V (*vs.* Li^+/Li).

The electrochemical impedance spectroscopy was carried out by using a frequency response analyzer Solartron 1253 connected to a potentiostat PAR 273 (EGG Instrument). The high stability of the transient measurement did not require a signal treatment, such as a filter. The impedance diagrams were plotted at different open-circuit voltages from the charged battery up to a complete discharged one. The frequency range was between 20 kHz and 5 mHz using 8 points per decade and the AC amplitude was 10 mV.

^7Li MAS NMR measurement.—The present ^{7}Li NMR spectra were recorded at 77.7 MHz and 4.7 T using a Bruker MSL 200 spectrometer. Magic angle spinning (MAS) was used with the spinning speed frequency range of 10–15 kHz in a commercial Bruker probe head. Due to the residual width of the signal in some cases, a solid echo sequence was applied with a synchronization of the interpulse delay to the rotor period. The pulse duration was fixed at 2.5 μs, leading to a flip angle close to 90°. The repetition time was maintained at 1 s. A 1 M solution of LiCl was used as an external reference. To determine the isotopic positions of the MAS pattern, the spinning speed was varied.

Table I. Relative proportion of Mn^{4+}/Mn^{3+}, average particle size, coordination number (CN), and bond distance of $LiMn_2O_4$ prepared at 250°C (method in Ref. 15 or 16) and 700°C (method in Ref. 15).

Sintering temperature		250°C	700°C
Surface C_{Mn}^{III+}		41.0%	50.5%
Surface C_{Mn}^{IV+}		59.0%	49.5%
Average particle size		~5 nm	~100 nm
(Mn-O)	CN	5.6	6.0
(Mn-O)	R (Å)	1.90(4)	1.91(5)
(Mn-Mn)	CN	5.2	6.0
(Mn-Mn)	R (Å)	2.88(9)	2.89(5)

Results

Nanocrystalline oxide $LiMn_2O_4$.—The first example concerns micro and nanocrystalline $LiMn_2O_4$. These crystallized spinel materials are known to present a satisfactory theoretical specific capacity.[13] However, studies mainly focused on the 4 V domain, because the capacity severely fades in the 3 V range. This decrease is due to the Jahn-Teller distortion, which leads to structural changes occurring when the average valence of Mn falls below +3.5.[13] The use of nanocrystalline material to overcome this shortcoming was first attempted by Bruce *et al.*[15] Comparative studies by scanning electron microscopy (SEM), transmission electron microscopy (TEM), X-ray photoelectron spectroscopy (XPS), and X-ray absorption spectroscopy (XAS) established that lowering the synthesis temperature decreases the particles size as expected but also increases the structural disorder and the average oxidation state of manganese (Table I). Moreover, the ratio Mn^{IV}/Mn^{III} is significantly higher at the surface than in the bulk.

A lowering of synthesis temperature down to 250°C exclusively leads to nanomaterials. This strongly modifies the ions chemical environment and their oxidation state at/near the grain surface. It also changes the electronic properties of the system stabilizing the energy of the surface *vs.* core Mn^{4+} ($3d_{eg}^0$) states, according to the schematic band model in Fig. 1. Therefore, the chemical bond strength of the first electrochemically inserted lithium ions is different when inserted in micro and nanocrystalline samples. The reduction of the surface-Mn^{4+} in nanocrystalline samples leads to Mn^{3+} and induces the 'electrochemical grafting' of Li^+ to maintain the electroneutrality of the material. To follow the evolution of the

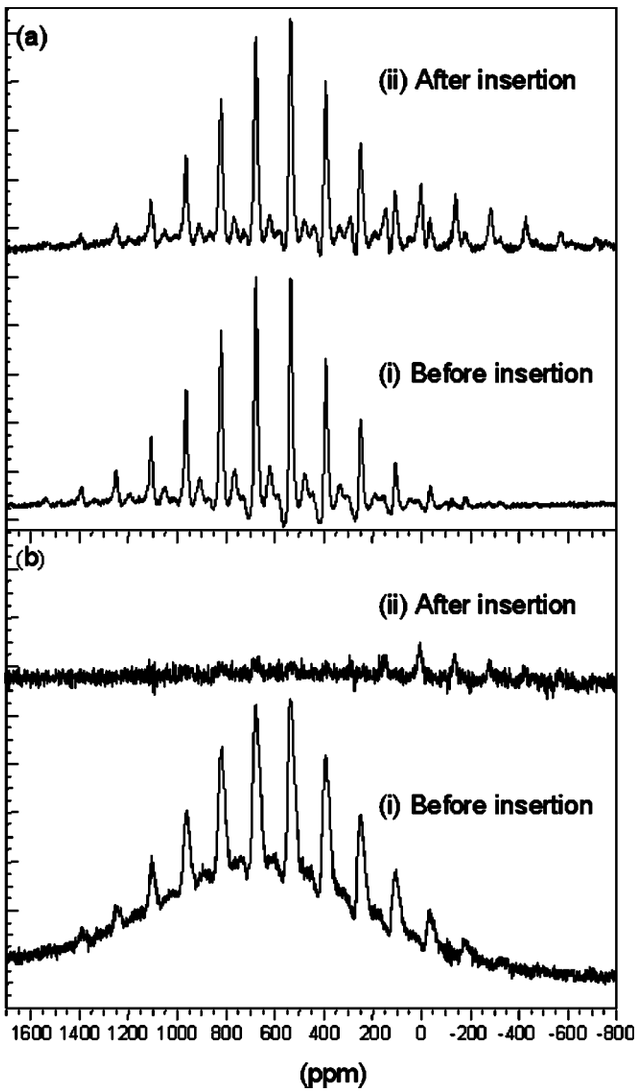

Figure 2. A comparison of ^{7}Li MAS NMR spectra (*i*) before and (*ii*) after the insertion of 0.15 mol Li^+ for (a) the microcrystalline 700°C sample (13) and (b) the nanocrystalline 250°C sample.[16]

chemical bond nature of the first inserted lithium, ^{7}Li MAS NMR studies were performed for both nanocrystalline and microcrystalline spinels before and after the insertion of only 0.15 mol of Li^+ (see Fig. 2).

While the Li^+ insertion does not induce any remarkable spectral change for the well-crystallized $LiMn_2O_4$[13] [Fig. 2a (*i* and *ii*)], it induces a dramatic suppression of the Li^+ NMR signal for the nanocrystalline one [Fig. 2b (*i* and *ii*)].[16]

Therefore, this Li^+ ion 'electrochemical grafting' process modifies the surface (as expected) as well as the electronic structure of the nanograins core. In agreement with the model, the nanocrystalline sample is the only one to show efficient cyclability in the 3 V region on a large range of cycles (200) as well as a smooth change of the Fermi-energy at the beginning of the insertion (Fig. 3).

Therefore, the grafting and consecutive insertion processes are reversible for the nanocrystalline $LiMn_2O_4$. In the same way, Goodenough *et al.* also showed that a simple ball-milling of well-crystalline spinel powders generated nanograins that contained significant intraparticular strain. These nanograins have a higher

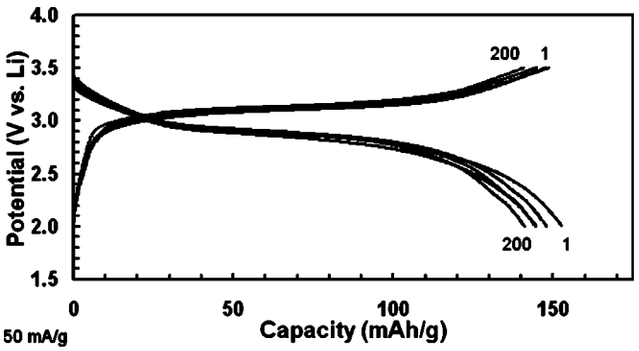

Figure 3. Charge-discharge profiles, in the 3 V domain, for nanocrystalline $LiMn_2O_4$ prepared at 250°C (applied current density of 50 mA/g).

manganese oxidation state than unmilled spinel particles, leading to an enhanced cycling performance in the 3 V range.[19]

Nanocrystalline oxide γ-Fe_2O_3 *and hybrid* γ-Fe_2O_3/*PPY* (*PPY = polypyrrole*).—The nanocrystalline oxide γ-Fe_2O_3 and nanohybrid γ-Fe_2O_3/PPY were chosen as another kind of materials. Bulk polypyrrole was also prepared for comparison. X-ray powder diffraction experiments show that the PPY/maghemite sample has the same crystal structure as maghemite meaning that treatment with pyrrole did not modify the core structure of the mineral oxide.[20,21] The composition of PPY/maghemite was deduced from thermal analysis and EPMA (electron probe microanalysis) and is estimated to be $Py_{0.07}Cl_{0.03}Fe_2O_3$, where Py abbreviates a pyrrole unit. The presence of Cl^- is due to the use of iron chloride for the synthesis. To estimate the quantity of polymer on the surface, a simple and rough calculation was performed as follows. Assuming a spherical particle with a diameter of 80 Å, the particle has a volume of 270 nm^3 containing 460 unit cells of maghemite. A unit cell contains $Fe_{64/3}O_{32}$, so a particle has 9800 Fe atoms. If the outermost shell has a thickness of *ca.* 2 Å, it has 1400 Fe atoms. From the composition $Py_{0.07}Cl_{0.03}Fe_2O_3$, a particle has 340 pyrrole units. Therefore, we believe that the polypyrrole does partially cover the surface of maghemite. The nature of interactions between maghemite, polypyrrole and Cl^- are still under investigation.

Figure 4 shows potential *vs.* capacity curves for the first discharge curves (2, 4, and 6) carried out in a galvanostatic mode at 8 mA/g in the voltage range of 1.3 to 4.3 V (*vs.* Li) for the nanocrystalline oxide (Fig. 4a), the hybrid γ-Fe_2O_3/PPY (Fig. 4b), and polypyrrole (PPY) (Fig. 4c).

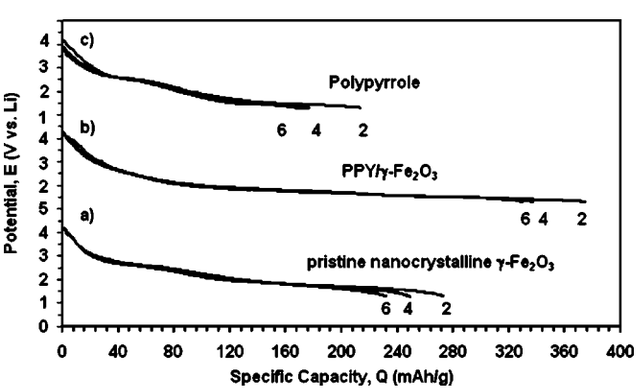

Figure 4. Variation of the voltage *vs.* Li (discharges curves 2, 4, 6) for the nanocrystalline pristine maghemite, the bare polypyrrole and the nanohybrid PPY/maghemite. The current density and potential range were 8 mA/g and 1.3-4.3 V.

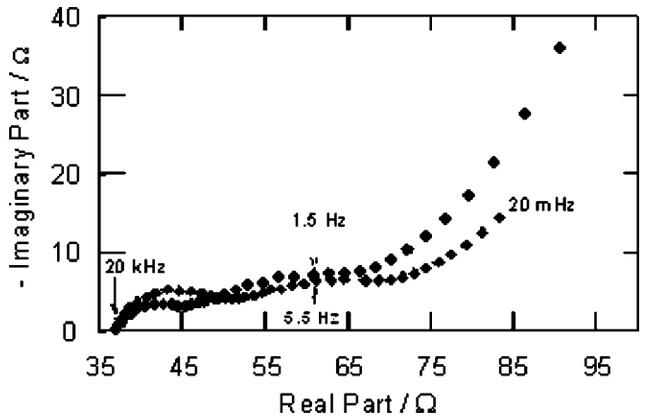

Figure 5. Electrochemical impedances for various discharge states of a lithium battery in the Nyquist plane. Nanocrystalline γ-Fe_2O_3 was used as working electrode. (●) E = 1.9 V *vs.* Li (♦) E = 1.7 V *vs.* Li.

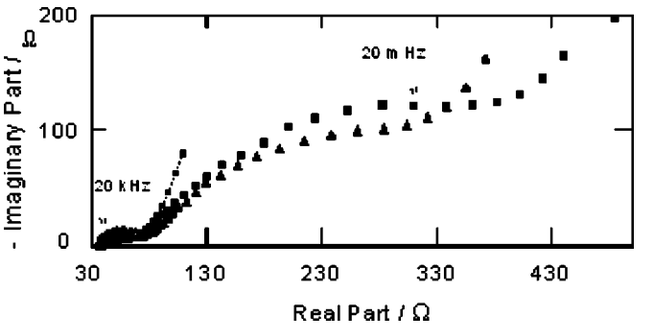

Figure 6. Electrochemical impedances for various discharge states of a lithium battery in the Nyquist plane. Nanocrystalline γ-Fe_2O_3 was used as working electrode. (●) E = 1.9 V *vs.* Li, (▲) E = 1.4 V *vs.* Li, and (■) E = 1.3 V *vs.* Li.

As already known, microcrystalline maghemite presents no electrochemical reversibility at room temperature.[20] This is not the case for nanocrystalline pristine maghemite, which exhibits a rather large capacity, in agreement with the model (Fig. 1) even if this capacity still decreases during the cycling.[22,23] Polypyrrole, also, shows a decrease of capacity after the sixth cycling. The influence of surface modification is clearly shown in Fig. 4b, which illustrates the overall electrochemical behavior of the nanohybrid sample and the changes induced by a surface modification such as the physisorption of PPY on nanograins surface. The potential decreases more smoothly for the nanohybrid sample and the capacity is somewhat stabilized after the sixth cycle (Fig. 4b).

To investigate the electrochemical mechanism involved during the charge-discharge of the lithium battery using nanocrystalline Fe_2O_3 as electrode material, electrochemical impedance spectroscopy (EIS) was employed. The EIS measurements were carried out for different open circuit voltages (OCV) from 3.5 V (*vs.* Li) down to 1.3 V (*vs.* Li). The highest potential corresponded to a nearly fully charged battery characterized thereby by a low rate of lithium in the Fe_2O_3 matrix. The lower potential was obviously attributed to a high rate of inserted lithium.

Figure 5 shows different diagrams in the Nyquist plane for two OCV. Three characteristic frequency domains were highlighted. A capacitive loop in the highest frequency range was attributed to the charge transfer reaction involved in the Li^+ insertion mechanism. The discharge of the battery generates the diffusion of Li^+ ions into the Fe_2O_3 matrix. This process led reduction reaction of Fe^{III} to Fe^{II}. This reduction is fast and can, therefore, be detected (capacitive loop) in the high frequency domain (Fig. 5). The middle frequency domain showed a second capacitive loop discussed below. The lowest frequency domain identified a pure capacitive process. This dynamical response was commonly observed in other works concerning diffusion processes into a semi-infinite electrode.[24] During the discharge process, the Li^+ ions diffused from the bulk toward the current collector through the γ-Fe_2O_3 electrode. The capacitive response in the lowest frequency range corresponds to the reversible accumulation of Li^+ ions at the interface between the current collector and the γ-Fe_2O_3 electrode. Figure 5 shows that the magnitude of the different responses increases when the open circuit voltage (OCV) decreases in agreement with other works using microcrystalline materials as insertion electrodes.[25-27]

Figure 6 shows the EIS curves for the lowest potentials corresponding to a high rate of lithium ion insertion. The high frequency loop continued increasing as already shown above. Moreover, the middle frequency domain exhibits a drastic increase of the magnitude of the capacitive loop. The Nyquist plots showed that the linear part defined for the highest frequencies of the middle frequency loop started with a 45° slope, which was attributed to a Warburg process. This typical response characterizes a diffusion process of Li^+ ions in the γ-Fe_2O_3 nanocrystalline electrode.

Thus, the EIS investigation characterized and separated the different elementary steps of the electrochemical process involved in the discharge process of the battery. The diagrams showed well-known responses leading thereby to identify the mechanism occurring during the Li^+ insertion in a nanocrystalline γ-Fe_2O_3 electrode as original material. The EIS investigations are still in progress.

Conclusion

Electrochemical measurements showed that the nanoparticles can be advantageously used to overcome kinetic problems in lithium insertion, and that the surface modification with PPY not only increases the capacity but also enhances reversibility of maghemite nanoparticles.

We have shown that the hybrid approach could also provide an innovative route for the development of novel and interesting functional materials with enhanced electrochemical activity.

The improved performances achieved with the hybrid γ-Fe_2O_3/PPY give a positive indication to the use of nanohybrid materials as lithium insertion electrodes and this aspect is under investigation. The strong electrochemical synergy effect observed is related to an efficient n-p junction at the core (γ-Fe_2O_3 being an n-type conductor)-shell (PPY being a p-type conductor) interface. Such a junction creates an electric field at the interface enhancing the migration of the lithium ions, from the electrolyte into the hybrid, and, thereby, strongly enhances the overall capacity. It is also clear that the nanocrystalline samples γ-Fe_2O_3 and $LiMn_2O_4$ exhibit larger capacities and better cyclability than their microcrystalline homologues. These experimental results illustrate and fit the proposed electrochemical model.

CNRS assisted in meeting the publication costs of this article.

References

1. K. Mizushima, P. C. Jones, P. J. Wiseman, and J. B. Goodenough, *Mater. Res. Bull.*, **15**, 783 (1980).
2. C. Delmas, C. Fouassier, and P. Hagenmuller, *J. Phys. Chem. Solids*, **39**, 55 (1978).
3. S. Levasseur, M. Ménétrier, E. Suard, and C. Delmas, *Solid State Ionics*, **128**, 11 (2000).
4. T. Nagura and K. Tozawa, *Prog. Batteries Sol. Cells*, **9**, 1209 (1990).
5. J. M. Tarascon, *Actualité Chim.*, **3**, 130 (2002).
6. S. Sarciaux, A. Le Gal La Salle, A. Verbaere, Y. Piffard, and D. Guyomard, *Mater. Res. Soc. Symp. Proc.*, **548**, 251 (1999).
7. L. I. Hill, R. Portal, A. Verbaere, and D. Guyomard, *Electrochem. Solid-State Lett.*, **4**, A180 (2001).
8. S. M. Haile, *Mater. Today*, **6**, 24 (2003).
9. G. Campet, S. J. Wen, S. D. Han, M. C. R. Shastry, J. Portier, C. Guizard, and L. Cot, *Mater. Sci. Eng., B*, **18**, 201 (1993), and references therein.
10. S. Y. Huang, G. Campet, N. Treuil, J. Portier, and K. Chhor, *Act. Pass. Elec. Comp.*, **19**, 189 (1996).
11. S. D. Han, S. Y. Huang, and G. Campet, *Act. Pass. Elec. Comp.*, **18**, 61 (1995).

12. G. Campet, J. Portier, B. Morel, and M. Bourel, *Act. Pass. Elec. Comp.*, **14**, 219 (1992).
13. J. B. Goodenough, M. M. Thackeray, W. I. F. David, and P. G. Bruce, *Rev. Chim. Miner.*, **21**, 435 (1984).
14. P. Gomez-Romero, *Adv. Mater. (Weinheim, Ger.)*, **13**, 163 (2001).
15. H. Huang and P. G. Bruce, *J. Electrochem. Soc.*, **141**, 76 (1994).
16. N. Treuil, J. Portier, G. Campet, J. Ledran, and J. C. Frison, European Pat. EP0837036 (1999); N. Treuil, C. Labrugere, M. Menetrier, J. Portier, G. Campet, A. Deshayes, J. C. Frison, S. J. Hwang, S. W. Song, J. N. Choy, *J. Phys. Chem. B*, **103**, 2100 (1999).
17. R. Massart, *IEEE Trans. Magn.*, **17**, 1247 (1981).
18. R. Massart, S. Neveu, V. Cabuil-Marchal, R. Brossel, J. M. Fruchart, T. Bouchami, J. Roger, A. Bee-Debras, J. N. Pons, and M. Carpentier, French Pat. 2662539. (1990).
19. S. H. Kang, J. B. Goodenough, and L. K. Rabenberg, *Chem. Mater.*, **13**, 1758 (2001).
20. C. W. Kwon, A. Poquet, S. Mornet, G. Campet, J. Portier, and J. H. Choy, *Electrochem. Commun.*, **4**, 197 (2002).
21. C. W. Kwon, S. J. Hwang, A. Poquet, N. Treuil, G. Campet, J. Portier, and J. H. Choy, in *New Trends in Intercalation Compounds for Energy Storage*, C. Julien, J. P. Pereira-Ramos, and A. Momchilov, p. 439, Kluwer Academic Publishers, Netherlands (2002).
22. X. S. Komaba, K. Suzuki, and N. Kumagai, *Electrochemistry (Tokyo, Jpn.)*, **7**, 506 (2002).
23. Y. J. J. Xu and G. Jain, *Electrochem. Solid-State Lett.*, **6**, A190 (2003).
24. J. Bisquert, G. Garcia-Belmonte, F. Fabregat-Santiago, and P. R. Bueno, *J. Electroanal. Chem.*, **475**, 152 (1999).
25. B. Markovsky, M. D. Levi, and D. Aurbach, *Electrochim. Acta*, **43**, 2287 (1998).
26. C. Wang, A. J. Appleby, and F. E. Little, *Electrochim. Acta*, **46**, 1793 (2001).
27. E. Barsoukov, J. H. Kim, J. H. Kim, C. O. Yoon, and H. Lee, *Solid State Ionics*, **116**, 249 (1999).